



Uncertainty assessment of Sentinel-2-retrieved vegetation spectral indices over Europe

S. De Petris, F Sarvia & E. Borgogno-Mondino

To cite this article: S. De Petris, F Sarvia & E. Borgogno-Mondino (19 Oct 2023): Uncertainty assessment of Sentinel-2-retrieved vegetation spectral indices over Europe, European Journal of Remote Sensing, DOI: [10.1080/22797254.2023.2267169](https://doi.org/10.1080/22797254.2023.2267169)

To link to this article: <https://doi.org/10.1080/22797254.2023.2267169>



© 2023 The Author(s). Published by Informa UK Limited, trading as Taylor & Francis Group.



Published online: 19 Oct 2023.



Submit your article to this journal [↗](#)



Article views: 325






View related articles [↗](#)



View Crossmark data [↗](#)

Uncertainty assessment of Sentinel-2-retrieved vegetation spectral indices over Europe

S. De Petris , F Sarvia  and E. Borgogno-Mondino 

Department of Agriculture, Forestry and Food Sciences (DISAFA), University of Torino, Grugliasco, Italy

ABSTRACT

Vegetation spectral indices (VIs) from multispectral remotely sensed imagery provide useful information in several sectors, especially if longing for change detection analyses or land monitoring. In this context, estimating uncertainty of VI values is crucial to recognize significant differences in both space and time domains. Unexpectedly, most applications reported in literature and involving VI do not take care about this issue, thus making unreliable a significant part of deductions. In this work, authors present an approach aimed at mapping in time and space the theoretical uncertainty of some widely used VIs basing their approach on the so-called variance propagation law (VPL). VPL can be consequently used to get an estimate of the theoretical VI uncertainty, starting from one of the bands involved in VI computation. VI uncertainty all along the year 2020 was then mapped at pixel level by Google Earth Engine over the whole Europe to test seasonal trends. Uncertainty of VI differences, as possibly resulting from a change detection approach, was tested by comparing monthly composites of VI and computing the expected uncertainty of differences along the year. An example was reported involving two NDVI maps (June–September) proving that about 30% of Δ VI were not significant.

ARTICLE HISTORY

Received 30 May 2023
Revised 29 September 2023
Accepted 1 October 2023

KEYWORDS

NDVI; NBR; NDRE;
uncertainty; Google Earth
engine; change detection



Introduction

Vegetation spectral indices (VIs) from multispectral remotely sensed imagery are known to provide useful information in several sectors, especially if longing for change detection analyses or land monitoring. VIs can, in fact, be proficiently used to derive precious information for many applications, including environmental monitoring, biodiversity conservation, phenological development, urban greening, natural disaster management and vigour/biomass vegetation dynamics assessment (Xue & Su, 2017). Specifically, in the agricultural and forestry sectors, they are compliant with large area monitoring requirements (Xiao & Moody, 2005; De Petris et al., 2021).

VI are obtained by mathematical combination of multispectral bands (at-the-ground reflectance calibrated) whose selection depends on the type of information one has to synthesize. Involved bands, generally, take into account reflectance differences that photosynthetically active plants show in the visible and near-infrared (NIR) spectral regions. These bands are known to be strongly correlated to plant biomass and prove to minimize soil/background and shadow-related effects; moreover, they can absorb most residual approximations related to the image

calibration and atmospheric correction (AC) process. This makes VIs able to provide a sort of standardized representation of vegetation that greatly improve monitoring and change detection deductions (Curran, 1981; Goward, 1989; Malingreau, 1989).

In 2014, the European Union (EU) launched the Copernicus program (Drusch et al., 2012) that greatly relies on Earth Observation satellite data that are expected to provide information useful for land cover/land use, climate change and disaster monitoring purposes (Malenovsky et al., 2012; Sentinel, 2014). In this framework, the multispectral instrument (MSI) on board of the Sentinel-2 A/B platforms (S2) can be retained, one of the best multispectral sensors providing free data with a worldwide coverage (Phiri et al., 2020). The main strengths of S2 data are: (i) red-edge band availability; (ii) medium-high geometric resolution (from 10 m to 60 m depending on the band); (iii) high temporal resolution, from 5 to 10 days (Drusch et al., 2012; Immitzer et al., 2016). These technical features appear to be particularly proper for vegetation monitoring and assessment over time. S2 data can be used to compute several VIs that can refer to different application fields like (a) biomass mapping in forestry (Anaya et al., 2009; Sinha et al., 2015) and in agriculture (Weiss et al., 2020); (b) plant disease assessment

CONTACT S. De Petris  samuele.depetris@unito.it  Department of Agriculture, Forestry and Food Sciences (DISAFA), University of Torino, Grugliasco 10095, Italy

© 2023 The Author(s). Published by Informa UK Limited, trading as Taylor & Francis Group.

This is an Open Access article distributed under the terms of the Creative Commons Attribution-NonCommercial License (<http://creativecommons.org/licenses/by-nc/4.0/>), which permits unrestricted non-commercial use, distribution, and reproduction in any medium, provided the original work is properly cited. The terms on which this article has been published allow the posting of the Accepted Manuscript in a repository by the author(s) or with their consent.

(Martinelli et al., 2015; Nilsson, 1995); (c) natural hazards like floods (De Petris et al., 2021; Sanyal & Lu, 2004), hail (Peters et al., 2000; Sarvia et al., 2020), drought (Wardlow et al., 2012; West et al., 2019), tree decline assessment (De Petris et al., 2020; Navarro et al., 2019) and storms (De Petris et al., 2021; McKean et al., 1991); (d) phenological assessment to classify and monitor crops (Xie et al., 2008); (e) land cover/land use mapping (Grabska et al., 2019; Guliyeva, 2020); (f) monitoring of climate change effects (Misra et al., 2020; Sarvia et al., 2021b); (g) supporting insurance-related issues (Sarvia et al., 2019, 2020); (h) vegetation water content assessment (Govender et al., 2007); (i) precision agriculture and precision forestry (Liaghat & Balasundram, 2010; Segarra et al., 2020); (l) supporting European Common Agricultural Policy controls (Kanjir et al., 2018; Sarvia et al., 2021).

According to literature (Karnieli et al., 2010; Xue & Su, 2017), the most widely used VIs from S2 data in the agricultural-forestry sector are the Normalized Difference Vegetation Index (NDVI), the Normalized Burn Ratio (NBR) and the Normalized Difference Red Edge index (NDRE). It is well known that most applications relying on these indices base their deduction on a multi-temporal approach (i.e. change detection or monitoring). NDVI was proposed by Rouse et al., (1974) and involved the NIR and red bands. It shows a high correlation with the Leaf Area Index (Wang et al., 2005; Zhang et al., 2012) proving its suitability in canopy and vegetation vigour characterization (Sripada et al., 2005) in space and time domains.

NBR (Chen et al., 2011; Escuin et al., 2008) was proposed for the identification and monitoring of vegetated water-stressed areas (burned areas). It is computed by combining bands from the NIR and mid-infrared regions (Filipponi, 2018; Quintano et al., 2018). Ordinarily, burned area analysis involving NBR could be performed by exploring cloudless images before and after the fire event (García & Caselles, 1991). NDRE (Fitzgerald et al., 2006) is proving to be highly effective in the precision farming context, being a good proxy of chlorophyll and nitrogen content of plants (Li et al., 2014). Its computation involves NIR and a red-edge band (Maes & Steppe, 2019).

Since most VIs are obtained as mathematical combination of bands (at-the-ground reflectance calibrated), they suffer from uncertainty whose strength depends on native band features. A proper estimate (and mapping) of VI uncertainty is crucial for a proper interpretation of VI and VI differences. In fact, if not considered, VI uncertainty can compromise reliability and meaning of deductions (Huemmrich & Goward, 1992; Price, 1992). While approaching VI uncertainty estimate,

one has to remember that reflectance of bands it relies on is itself a derived measure that is obtained through the application of a proper radiative transfer model – RTM (Vermote et al., 1997). RTM is in charge of recovering an adequate estimate of the local at-the-ground reflectance from the raw data through an image calibration step that includes AC. RTM is a mathematical model that necessarily propagates all uncertainties affecting involved measures. These can be related to: a) accuracy of the sensor calibration functions; b) radiometric sensitivity of sensor; c) atmospheric parameters, viewing geometry, Earth–Sun distance coefficient; d) Sun irradiance. All these factors make reasonable to doubt about the accuracy of reflectance involved in VI computation and suggest to carefully consider the possibility of giving a local estimate of VI uncertainty taking care about one of the involved bands. Nevertheless, most applications using spectral indices do not consider, neither quantify, VI uncertainty. This unfavourable practice is partially due to the nature of the index itself; in fact, in most cases, there are not reference data for a-posteriori validation, which can only be achieved by comparing some image-derived sample estimates with the corresponding ground surveyed ones (Beck et al., 2007; Borgogno-Mondino et al., 2016). This would require costly and time-consuming ground campaigns by spectroradiometers that would have to be performed simultaneously to image acquisition. These operations cannot be achieved for most applications and certainly are no longer possible for past images. Consequently, the only possibility is moving to the computation of a theoretical (expected) uncertainty (possibly underestimating the actual one) of the final product.

With these premises, this work is specifically aimed at suggesting an operational approach to estimate and map VI uncertainty (in space and time) at European level. The above-mentioned VIs (NDVI, NBR and NDRE) were considered as representative of a wider group of S2-derived indices. Consequently, the proposed methodology can be applied to all similar computation concerning other spectral indices. Estimates were achieved by considering the nominal uncertainty of bottom of the atmosphere (BOA) reflectance from Level 2A S2 images.

Materials and methods

Study area

This work is intended to provide a tool for easily mapping VI uncertainty in space and time. Nevertheless, it was also intended for providing

a preliminary evaluation of the European continental context, looking for eventual dependencies of VI accuracy from position and season. Consequently, the application of the proposed model for VI uncertainty estimate was applied with reference to a study area [area of interest (AOI)] corresponding to the whole European continent (Figure 1). According to the European Environment Agency, Europe is covered for more than 48% by forest and semi-natural areas and for about 41% by agricultural areas (www.eea.europa.eu). Consequently, it is reasonable to assume that AOI correspond to a high vegetated landscape (about 90%), which makes it suitable for large-scale VI analysis.

Four EU countries (Greece, Czech Republic, Lithuania and Finland) were additionally selected as focus areas (FAs) as representative of different, but paradigmatic, vegetation landscapes developing at different latitudes. Land cover classes at 2018 derived by CORINE land cover (Büttner, 2014) project and correspondent areas are reported in Table 1 for FAs. FAs were selected to have very similar longitude but different latitude (they

are located along the north–south direction). Two different analyses were performed over EU and FAs. One aimed at assessing spatial and temporal variability of VIs and their uncertainty over the whole Europe. The second one is aiming at testing the presence of a latitudinal gradient of NDVI uncertainty and how the average VI uncertainty temporal behaviour was significantly different along this gradient.

Available data

Presently, a large amount of remotely sensed data from public and open archives can be accessed and managed by advanced cloud computing services like Google Earth Engine – GEE (Gorelick et al., 2017; Mutanga & Kumar, 2019). This largely facilitates the analysis of long time series making easier the processing of multispectral imagery at continental or global scale. Within this framework, after modelling VI uncertainty, the same model was applied to the whole Europe implementing a specific routine in GEE relying on GEE available datasets.

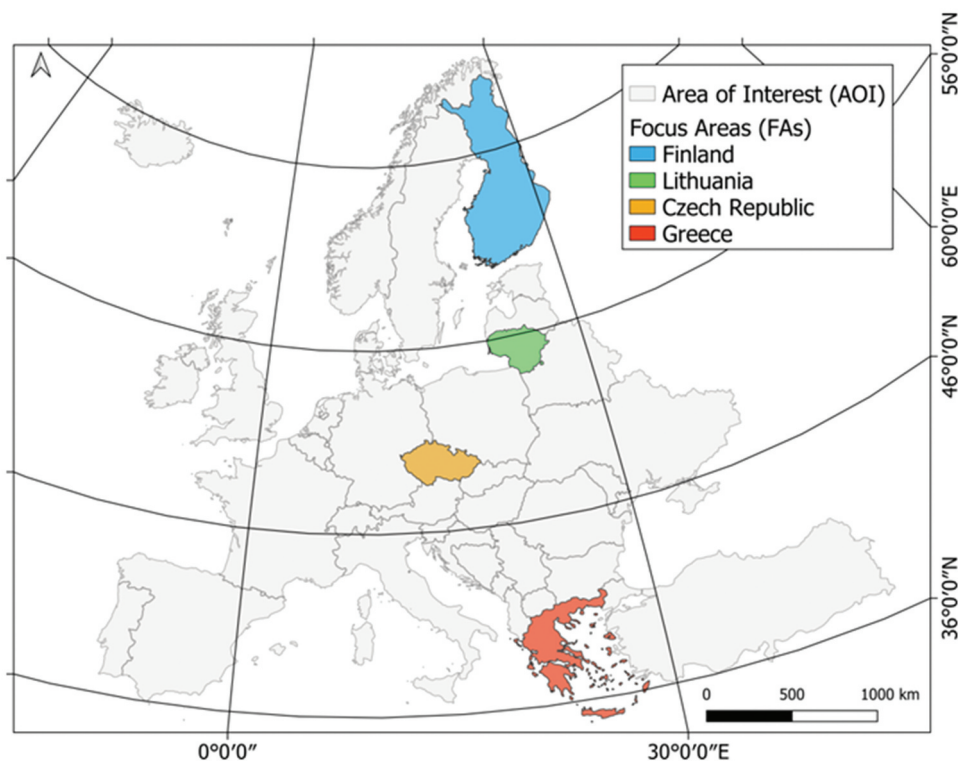


Figure 1. Study area and focus area overview. Reference frame: WGS84.

Table 1. Land cover classes and size according to CORINE land cover (2018) for FA (%).

Countries (code)	Artificial surfaces	Agricultural areas	Forest and semi natural areas	Wetlands	Water bodies
Greece (GR)	3.29	38.82	56.31	0.47	1.11
Czech Republic (EZ)	6.71	56.77	35.65	0.14	0.73
Lithuania (LH)	3.43	58.42	34.72	0.87	2.56
Finland (FI)	1.41	8.3	74.53	6.32	9.44

Sentinel-2 Level 2A dataset

For this work, averagely 75 Sentinel-2 (S2) Level-2A images per tile were collected covering the period 1 January–31 December 2020. S2 Level 2A products from GEE were provided BOA calibrated, making them suitable for land applications (Louis et al., 2019; Main-Knorn et al., 2017; Phiri et al., 2020). The “scene classification layer” (SCL) supplied with the images was also obtained for recognizing and masking out “unreliable” pixels (i.e. cloudy, shadowy and failed pixels) during VI computation. In Table 2, the main technical features of the S2 MSI are reported.

S2 Level 2A data refer about BOA reflectance. Reference values for the uncertainty of reported reflectance measures can be found from reports of the Atmospheric Correction Inter-comparison eXercise (ACIX) (Doxani et al., 2018; Vermote et al., 2019). ACIX is an international initiative of the Committee on Earth Observation Satellites, the National Aeronautics and Space Administration and the European Space Agency aimed at analyzing surface reflectance (SR) products as obtained through various state-of-the-art AC processors, with special concerns about Landsat-8 and Sentinel-2 image datasets. Analyses are based on calibration sites located all around the world. In particular, 19 ACIX sites were selected based on the locations of the international Aerosol Robotic Network (AERONET) taking care of the different climatic zones and land cover types. The network provides a reliable, globally representative and consistent dataset of atmospheric variables that can be used for validating performances of AC processors (Holben et al., 1998; Smirnov et al., 2000). Within the ACIX project, the AERONET in-situ measurements were assumed as ground truth for reflectance validation. BOA reflectance values of S2 Level-2A dataset obtained by the Sen2Cor processor (Louis et al., 2016) were compared by difference with the reference dataset. This was obtained applying the 6S radiative transfer code (Vermote et al., 1997) fed with atmospheric measures from AERONET. The comparison was achieved at band level making possible to retrieve different reference values of uncertainty for the S2 Level-2A

reflectances, depending on the band. Reference values of reflectance uncertainty were obtained from about 3 million of pixels around the world. Figure 2 show spectral uncertainties ($\sigma_{\rho\lambda}$) of the S2 Level-2A bands as reported by ACIX (Doxani et al., 2018).

Land cover

The Copernicus Global Land Service Land Cover Map v3.0.1 (CGLC) is the global land cover product having the highest geometric resolution (100 m) available in GEE. CGLC is a raster layer derived by PROBA-V imagery that is provided for the period 2015–2019. CGLC maps 22 land cover classes. The declared average class accuracy (producer’s accuracy) is about 80% (Buchhorn et al., 2020). In this work, only vegetated classes were considered. Native classes were therefore preventively merged into macro-classes according to the scheme of Table 3.

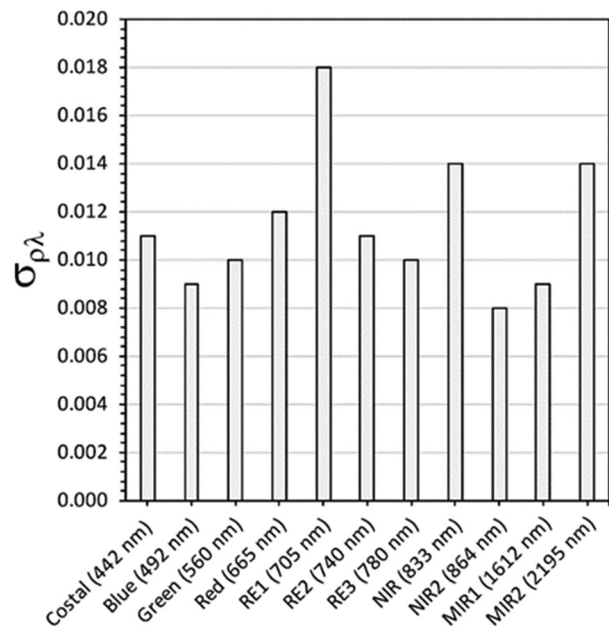


Figure 2. Uncertainties of BOA reflectance for S2 level-2A bands as reported by ACIX (Doxani et al., 2018).

Table 2. Sentinel-2 multispectral instrument technical features.

Sentinel-2 bands	Central wavelength (nm)	Bandwidth (nm)	Spatial resolution (m)
B1	442	21	60
B2	492	66	10
B3	560	35	10
B4	665	31	10
B5	705	15	20
B6	740	15	20
B7	780	20	20
B8	833	106	10
B8A	864	21	20
B9	945	20	60
B10	1375	31	60
B11	1612	92	20
B12	2195	180	20

Temporal resolution: 5–10 days; radiometric resolution: 12 bit.

Table 3. Copernicus Global Land Service Land Cover Map.

CGLC	Class code in GEE	Merged classes
Forest	111-112-113-114-115-116-121-122-123-124-125-126	Vegetated areas
Shrubs	20-30	
Croplands	40	
Herbaceous wetland	90	
Bare/sparse vegetation	60	
Lichen/moss	100	Other areas
Snow/ice	70	
Built-up	50	
Permanent water	80-200	

Data processing

The workflow adopted in this work is summarized in Figure 3. A first part concerns the definition of a model to estimate VI uncertainty. This model is then applied to S2 data and uncertainty maps generated in GEE. The second part concerns the assessment over the Europe of temporal patterns of the uncertainty maps. The last step shows a practical example of proposed method to detect significant from not significant VI variations while working within change detection or time series-based approaches.

Modelling the theoretical uncertainty of VIs and its effects in change detection

Low-cost validations aimed at testing actual accuracy of mapped VI values from satellite data are not possible. In fact, validation relies on the comparison between a reference dataset (ground truth) and

model estimates. The crucial point of this desirable approach is that ground surveys based on the adoption of a spectroradiometer are required to generate the reference dataset. Even though this was achievable (albeit expensive) for ongoing acquisitions, it would not be longer practicable for the past ones. The alternative is to refer to the theoretical uncertainty that could affect the final (“indirect”) measure (VI) taking care of the contribution of those “direct” measures (SR) that participate to the model. With special concerns about VI, their theoretical uncertainty can be estimated if the one affecting the involved bands is somehow known. The reference statistical tool suitable for this task is the variance propagation law (VPL – Equation 1). VPL permits to estimate the theoretical variance of the dependent variable y , from one of the independent ones (x_i) that participate to its computation.

$$\sigma_y^2 = \left(\frac{\partial y}{\partial x_1}\right)^2 \cdot \sigma_{x_1}^2 + \left(\frac{\partial y}{\partial x_2}\right)^2 \cdot \sigma_{x_2}^2 + \dots + \left(\frac{\partial y}{\partial x_n}\right)^2 \cdot \sigma_{x_n}^2 \quad (1)$$

where $y = f(x_1, x_2, \dots, x_n)$ is the dependent variable, x_i the independent ones and $\sigma_{x_i}^2$ their variance (supposed known). While applying VPL to VIs, the local value (pixel by pixel) of the partial derivatives of VI with respect to the involved bands (independent variables) has to be computed.

To properly use VPL, one must first precisely specify the model formula to which it must be applied. In this work, three common adopted VIs, namely, NDVI, NBR and NDRE were used, and their formulas are reported in Equations 2-4.

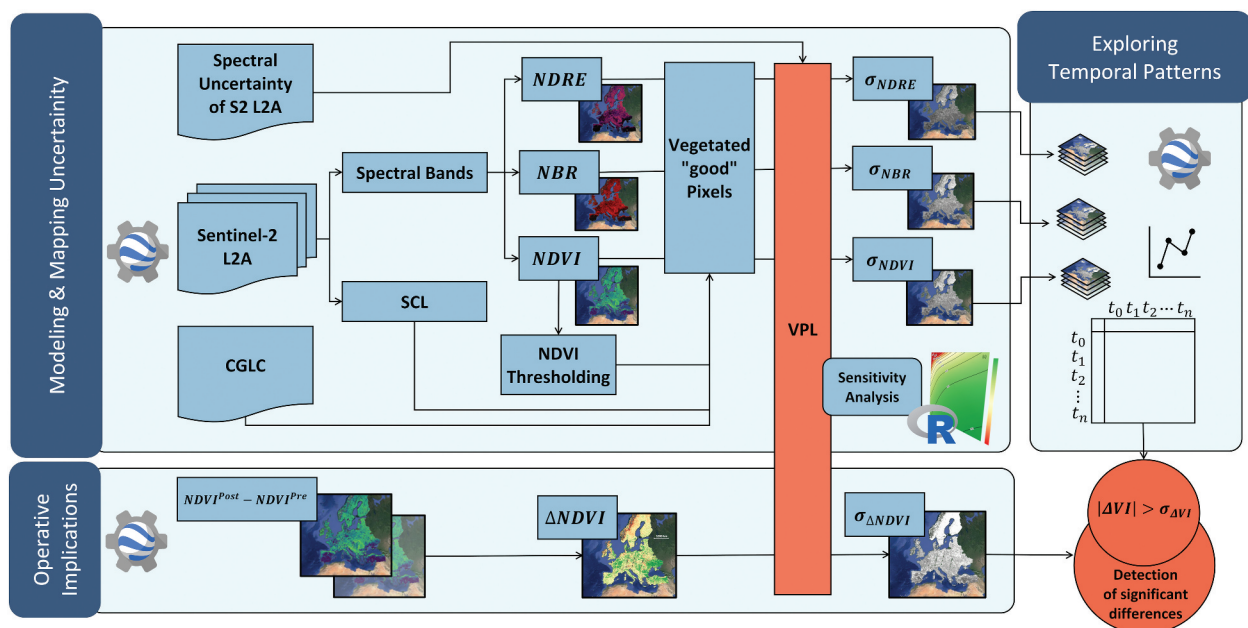


Figure 3. Workflow adopted in this work. A model to estimate VI uncertainty was proposed based on the variance propagation law (VPL) and implemented in GEE involving S2 images. Sensitivity analysis was also performed in R environment to assess how different bands combination can affect the uncertainty. Then, temporal patterns of VI uncertainty for selected indices were explored over both whole EU and FAs. Finally, to highlight operative implications of proposed approach, two NDVI images were compared by difference and using VPL a detection of significant differences was performed.

$$NDVI = \frac{\rho_{NIR}(x, y) - \rho_{RED}(x, y)}{\rho_{NIR}(x, y) + \rho_{RED}(x, y)} \quad (2)$$

$$NBR = \frac{\rho_{NIR}(x, y) - \rho_{MIR2}(x, y)}{\rho_{NIR}(x, y) + \rho_{MIR2}(x, y)} \quad (3)$$

$$NDRE = \frac{\rho_{NIR}(x, y) - \rho_{RE1}(x, y)}{\rho_{NIR}(x, y) + \rho_{RE1}(x, y)} \quad (4)$$

where $\rho_i(x, y)$ is the SR value of i -th spectral band at a generic position (x, y) .

Successively, SR uncertainty has to be propagated along index calculation. Finally, VI uncertainty at a given position, $\sigma_{VI}(x, y)$, can be estimated applying Equation 1 to Equations 2–4 (Equations 5–7):

$$\sigma_{NDVI}(x, y) = \sqrt{\left(\frac{2 \cdot \rho_{RED}(x, y)}{[\rho_{RED}(x, y) + \rho_{NIR}(x, y)]^2}\right)^2 \cdot \sigma_{\rho_{NIR}}^2(x, y) + \left(-\frac{2 \cdot \rho_{NIR}(x, y)}{[\rho_{NIR}(x, y) + \rho_{RED}(x, y)]^2}\right)^2 \cdot \sigma_{\rho_{RED}}^2(x, y)} \quad (5)$$

$$\sigma_{NBR}(x, y) = \sqrt{\left(\frac{2 \cdot \rho_{MIR2}(x, y)}{[\rho_{MIR2}(x, y) + \rho_{NIR}(x, y)]^2}\right)^2 \cdot \sigma_{\rho_{NIR}}^2(x, y) + \left(-\frac{2 \cdot \rho_{NIR}(x, y)}{[\rho_{NIR}(x, y) + \rho_{MIR2}(x, y)]^2}\right)^2 \cdot \sigma_{\rho_{MIR2}}^2(x, y)} \quad (6)$$

$$\sigma_{NDRE}(x, y) = \sqrt{\left(\frac{2 \cdot \rho_{RE1}(x, y)}{[\rho_{RE1}(x, y) + \rho_{NIR}(x, y)]^2}\right)^2 \cdot \sigma_{\rho_{NIR}}^2(x, y) + \left(-\frac{2 \cdot \rho_{NIR}(x, y)}{[\rho_{NIR}(x, y) + \rho_{RE1}(x, y)]^2}\right)^2 \cdot \sigma_{\rho_{RE1}}^2(x, y)} \quad (7)$$

where $\rho_i(x, y)$ is the BOA reflectance map of i -th spectral band; $\sigma_{VI}(x, y)$ is the uncertainty map of specific VI; σ_{ρ_λ} is the SR uncertainty at λ -th wavelength. It is worth to notice that the latter values are specific for the adopted multispectral sensor and depend also on AC and RTMs adopted. In this work, S2 σ_{ρ_λ} were the ones reported in Figure 2.

What is interesting in Equations 2–7 is that all computations are dependent from local values. Therefore, to give evidence of VI uncertainty sensitivity from the involved band values, some simulations were performed through a self-developed routine developed in R vs. 4.1. by progressively varying band values within their existence range (0.00–1.00, with

a 0.01 step). This sensitivity analysis was performed in order to explore how the combination of different reflectance values affect VI uncertainty. In particular, NDVI, NBR and NDRE simulations were run assuming as reflectance uncertainty values the ones reported in Figure 2. These scenarios allow to explore the theoretical behaviour of VPL application to VIs, looking for all possible SR value combinations.

Despite theoretical analysis, in this work, practical implication of uncertainty was also explored. In fact, it is worth to remind that, while facing a change detection or time series-based problem where two VI maps of different dates are compared by difference (Equation 8), VPL has to be further applied to the difference itself to locally get an estimate of its theoret-

tical uncertainty, $\sigma_{\Delta VI}(x, y)$.

$$\Delta VI(x, y) = VI_{t+\Delta t}(x, y) - VI_t(x, y) \quad (8)$$

where VI_t is the VI value at the date t (ante), and $VI_{t+\Delta t}$ is the VI value at a later date (post).

To make evident operational consequences of this approach, change detection comparing VI maps at different times was considered. VPL was therefore applied to the VI difference (ΔVI), and the correspondent formula obtained (Equation 9).

$$\sigma_{\Delta VI}(x, y) = \sqrt{[\sigma_{VI}(t + \Delta t, x, y)]^2 + [\sigma_{VI}(t, x, y)]^2} \quad (9)$$

where $\sigma_{VI}(t, x, y)$ and $\sigma_{VI}(t + \Delta t, x, y)$ are the previously mapped VI uncertainty at the date t (ante) and $t + \Delta t$ (post), respectively. It is clear that $\sigma_{\Delta VI}(x, y)$ depends on uncertainties of the two compared VI maps. From a practical point of view, it is possible to define which index differences can be considered meaningful and which are not within change detection or time series analysis. To detect significant changes (differences), $SD(x, y)$, condition $|\Delta VI(x, y)| > \sigma_{\Delta VI}(x, y)$ can be locally tested. In order to stress the practical implications of the proposed approach, we, finally, used the previously generated information to map significant and non-significant VI changes. In this framework, $\sigma_{\Delta VI}(x, y)$ represents the sensibility for appreciating local index changes. Index differences lower than $\sigma_{\Delta VI}(x, y)$ can be labelled as not significant, stating that, at that position, nothing really changed.

Mapping VI and its uncertainty in Europe through GEE

NDVI, NBR and NDRE maps from S2-L2A images were computed over Europe within GEE. During computation, three masking steps were achieved: (i) one aimed at masking out unreliable pixels as mapped in the SCL layer (i.e. clouds, cloud shadows, cirrus and snow cover); (ii) one aimed at masking out pixels belonging to non-vegetated classes (as mapped in CGLC); (iii) one aimed at masking out pixels having an NDVI value < 0.3 (Burgan, 1993; Gao, 1996; Ormsby et al., 1987; Zhang et al., 2003). This condition was tested separately for all processed dates, thus permitting to selectively consider, or not consider, the pixel depending on its vegetative state along the year. The basic idea is to exclude a vegetated pixel when it doesn't show an active phenological state (i.e. during its leaf-off period). Focusing on remaining pixels, VPL was locally applied for all VI maps according to Equations 5–7, thus permitting to map VI uncertainty (σ_{VI}) over Europe at the different dates. To synthesize results, both VI and σ_{VI} image time series were monthly averaged and mosaicked. This composite strategy was applied in order to guarantee that the whole Europe have at least one image within the same month. At the end, a total of 12 VI and σ_{VI} maps were generated and stacked for the 3 considered VIs.

In order to make evident the effectiveness of mapping $\sigma_{\Delta VI}$ by VPL, the corresponding maps were generated with reference to the monthly averaged VI images. All possible combinations among months were considered to explore $\sigma_{\Delta VI}$ dependence from compared dates. Europe averaged values were computed to synthesize this type of information and tabled. This analysis can be used to find the change detection combination along the year able to minimize

$\sigma_{\Delta VI}$, and, consequently, to maximize reliability of detected changes.

To exemplify the process, with reference to two monthly averaged NDVI images (namely, June 2020 and September 2020), the correspondent $\Delta NDVI(x, y)$, $\sigma_{\Delta NDVI}(x, y)$ and $SD(x, y)$ maps were generated. Some statistics concerning the number of significantly and non-significantly changed vegetated pixels were computed for the whole Europe.

Exploring temporal pattern of VI uncertainty in Europe

With reference to the above-mentioned σ_{VI} and VI image time series (monthly averaged), the corresponding global (for the entire Europe) mean and standard deviation values were computed for all months and graphed to show their temporal trends.

To partially investigate if the average values were representative of the whole Europe, solely considering NDVI, in spite of any local peculiarity, the global mean and standard deviation values were compared with the ones coming from FAs.

Results

Modelling the theoretical uncertainty of VIs and its effects in change detection

According to the general formulation of VPL (Equation 1) and with reference to the selected VIs (NDVI, NBR, NDRE), the correspondent formulas were computed and applied at pixel level to map VI uncertainty, $\sigma_{VI}(x, y)$. To properly show the effects of the above-mentioned relationships relating BOA reflectances to VI uncertainty, some simulations were run. Reflectance values of involved bands were progressively changed from 0.01 to 1 with a step of 0.01, and the correspondent VI value and VI uncertainty values were computed. During simulations, uncertainty of involved bands ($\sigma_{\rho\lambda}$) was assumed equal to the one proposed by ACIX (see Figure 2). Specifically, the following values were adopted: $\sigma_{\rho RED} = 0.012$, $\sigma_{\rho NIR} = 0.014$, $\sigma_{\rho MIR2} = 0.014$, $\sigma_{\rho RE1} = 0.018$. Simulations showed that σ_{VI} tends to decrease when the reflectance of involved bands increases (Figure 4). This suggests that VI appears to be more accurate for highly reflecting surfaces. Moreover, it can be noted that the same VI value can correspond to different reflectance values of the involved bands. Consequently, one can obtain different uncertainty values for the same VI value. Specifically, according to Figure 4a, it can be highlighted that a σ_{NDVI} value of 0.03 can be obtained in different ways: i) by very high reflectance values in the σ_{RED} (e.g. equal to 0.9) and very low in the σ_{NIR} (e.g. between 0 and 0.1); ii) by very low reflectance values in the RED band ($0 < \sigma_{RED} < 0.1$)

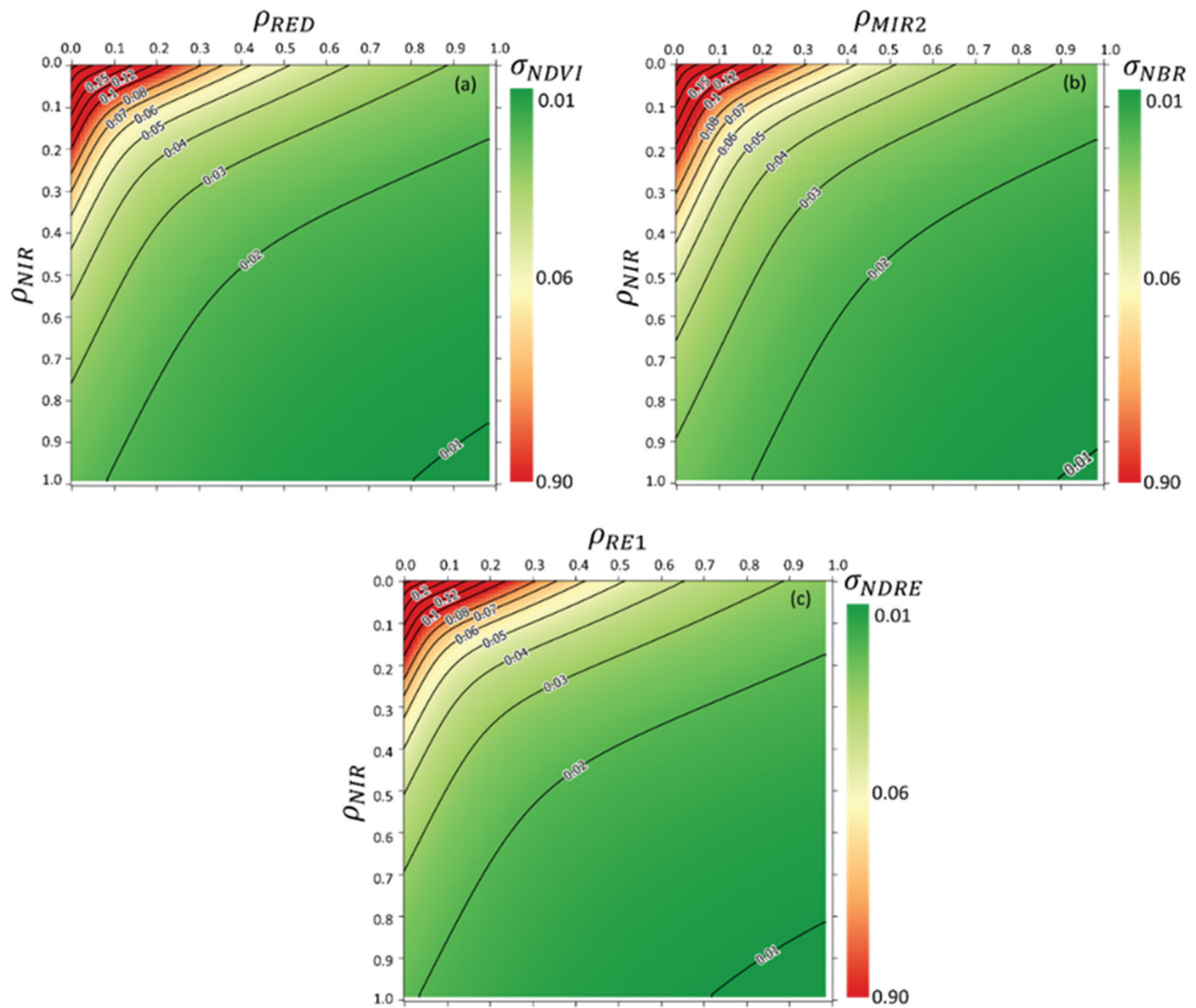


Figure 4. Graphs relating theoretical σ_{Vis} with reflectance of the bands used for VI computation. (a) σ_{NDVI} ; (b) σ_{NBR} ; (c) σ_{NDRE} .

and very high in the NIR (σ_{NIR} greater than 0.7); iii) by average reflectance values of NIR and RED (both reflectance values around 0.3). Similar behaviour can also be observed in Figure 3(b),(c) corresponding to σ_{NBR} and σ_{NDRE} , respectively.

This makes evident that the main driver of VI accuracy is not the VI itself but the reflectance values of the participating bands. Operationally speaking, when mapping VI uncertainty, it will be necessary to go back to the reflectance values of involved bands, that, consequently, have to be obtained together with the VI. This has to be carefully considered when programming services for providing ready-to-use products (e.g. NDVI maps).

Mapping VI and its uncertainty in Europe by GEE

To give a practical example, aimed at proposing an operational scenario, the above-mentioned concerns were applied over Europe for the year 2020 using GEE and developing an appropriate routine. This operates different tasks. The first one is aimed at masking out unreliable and not vegetated pixels. This was obtained

intersecting information from CGLC and SLC coupled with a thresholding step based on the instantaneous NDVI value (0.3). The latter allows to not consider areas temporarily not covered by vegetation trying to mitigate effect of not vegetated pixels (bare soils). It is worth to stress that these masking steps are strongly dependent on the accuracy of adopted layers. However, masks do not directly affect VI uncertainty since they are not involved in its computation, but they may only affect summary statistics at the continental level.

A second task concerns the computation, at pixel level, of the monthly mean value of NDVI, NBR and NDRE. A third task concerns the computation of the associated theoretical uncertainty. An example, showing VI and VI uncertainty maps for a winter and summer situations, is presented in Figure 5. According to expectations and literature (Potter & Brooks, 1998), NDVI values appear to be lower in winter than in summer (Figure 5a,b). Conversely, uncertainty of NDVI (Figure 5c,d) appears to be lower in summer and higher in winter. Similar results can be observed for NBR and NDRE, as well. VI

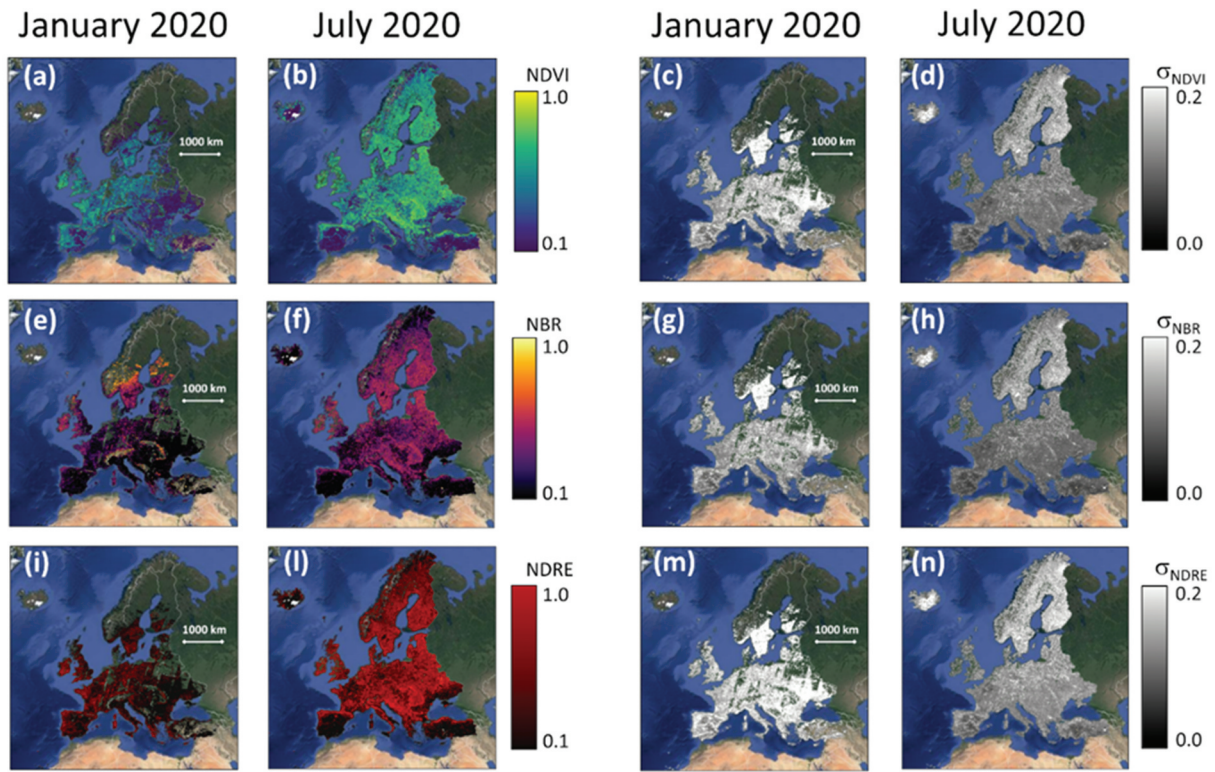


Figure 5. Winter VI mosaic over EU (a, e, i) and relate uncertainty (c, g, m). Summer VI mosaic over EU (b, f, l) and relate uncertainty (d, h, n). All images were computed directly on GEE.

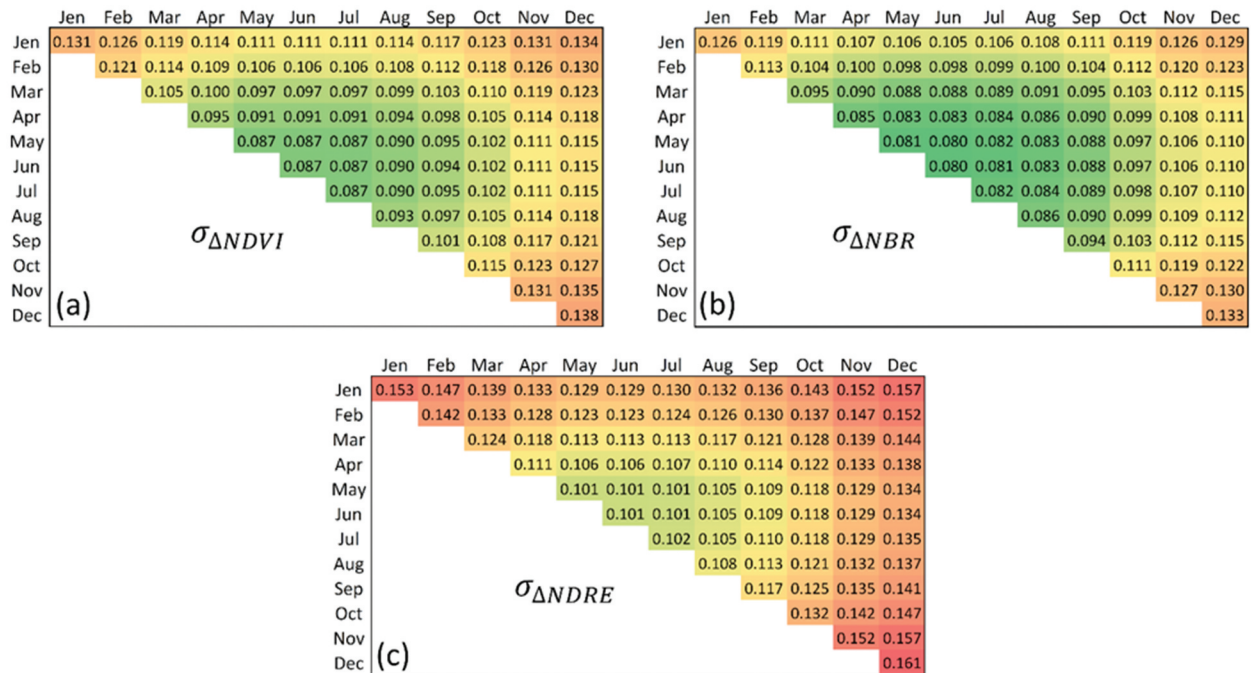


Figure 6. European average values of $\sigma_{\Delta VI}$ computed for all possible month combinations. a) $\sigma_{\Delta NDVI}$; b) $\sigma_{\Delta NBR}$; c) $\sigma_{\Delta NDRE}$.

values, in fact, result to be higher in July (Figure 5f-l) and lower in January (Figure 5e-5i); uncertainty was found to be higher in the winter period (Figure 5g-m) and lower in the summer period (Figure 5h-n).

As far as effects of VI uncertainty can generate in change detection applications, one has to consider that both VI uncertainty of the two compared

dates, $\sigma_{VI}(t, x, y)$ and $\sigma_{VI}(t + \Delta t, x, y)$, play to determine the final uncertainty of VI difference, $\sigma_{\Delta VI}(x, y)$, according to VPL (Equations 3–5). It is worth to remind that $\sigma_{\Delta VI}(x, y)$ locally varies depending on local VI uncertainty and, therefore, on reflectance values of the bands defining the index.

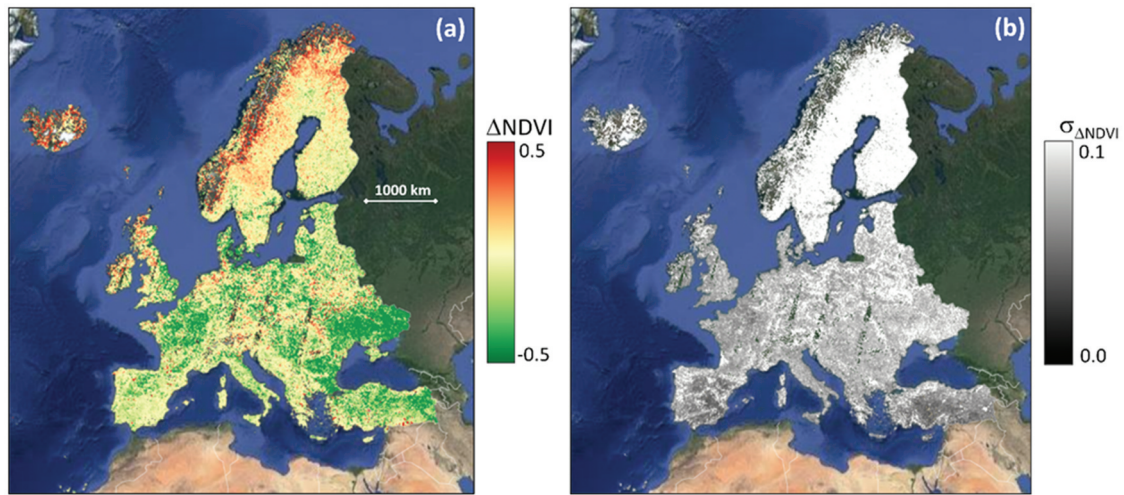


Figure 7. (a) $\Delta NDVI(x, y)$ involving 2020 September and July difference; (b) $\sigma_{\Delta NDVI}(x, y)$ derived by applying Equation 3 to $\Delta NDVI(x, y)$.

A result able to give a general overview of this phenomenon is difficult to be given. The authors tried to synthesize potentialities of $\sigma_{\Delta VI}(x, y)$, referring to the European average values of $\sigma_{\Delta VI}(x, y)$ computed for all possible differences between monthly averaged values of VIs for the year 2020. The results are reported in Figure 6. It can be noted that, if winter acquisitions participate to the difference, higher $\sigma_{\Delta VI}$ values can be found. It is authors' opinion that tables of Figure 6 could be eventually used as a rough tool able to preliminarily give an estimate of the average expected $\sigma_{\Delta VI}$ value in Europe, depending on the compared months. It is worth to stress that the values reported in Figure 6 are averaged over the entire Europe; consequently, local $\sigma_{\Delta VI}$ values could be surprisingly different from the estimated average ones.

To make explicit the operational added value of this approach, two monthly averaged NDVI maps over Europe (namely, June 2020 and September 2020) were compared by differencing and the correspondent $\sigma_{\Delta NDVI}$ mapped. This was used to separate significant from non-significant differences. Figure 7a shows the NDVI difference, $\Delta NDVI(x, y) = NDVI_{Jun}(x, y) - NDVI_{Sep}(x, y)$; Figure 7b shows the uncertainty of difference, i.e.

$\sigma_{\Delta NDVI}(x, y)$. It can be noted that Northern Europe suffers from a higher uncertainty that could be probably caused by a general lower NDVI signal in September associated with the local boreal vegetation (J. M. Chen, 1996).

While testing significance of changes, the two generated maps, i.e. $\Delta NDVI(x, y)$ and $\sigma_{\Delta NDVI}(x, y)$, were locally compared testing the condition $\Delta NDVI(x, y) > \sigma_{\Delta NDVI}(x, y)$. Only pixels satisfying this condition $SD(x, y)$ can be retained that significantly changed in the reference period. According to the above-mentioned example, the authors found that for vegetated pixels (about 60% of the whole image), only 35.7% showed significant changes.

Exploring temporal pattern of VI uncertainty in Europe

Concerning temporal pattern of VI uncertainty, its European average and standard deviation (in the space domain) temporal trends were computed for all considered spectral indices (Figure 8). The results confirm that VI uncertainty is higher in winter and lower in summer for all VIs. Spatial variability (i.e. standard deviation value at European level) of VI uncertainty appears to be higher in winter (greater

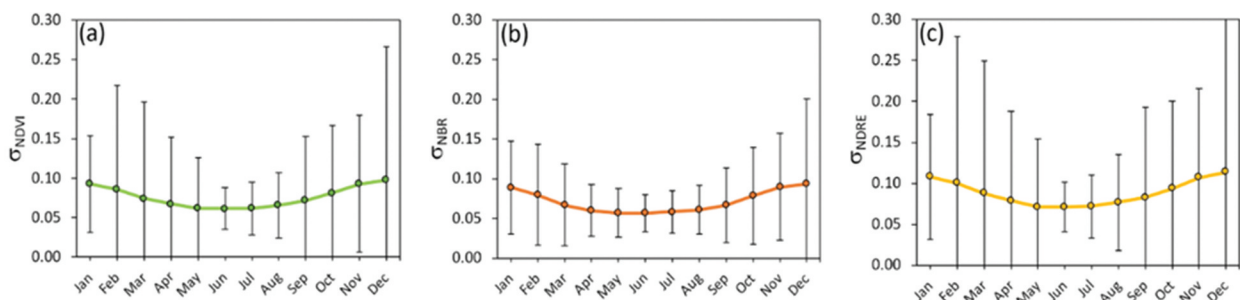


Figure 8. Temporal variability of σ_{VI} s and the spatial standard deviation over EU. (a) σ_{NDVI} ; (b) σ_{NBR} ; (c) σ_{NDRE} .

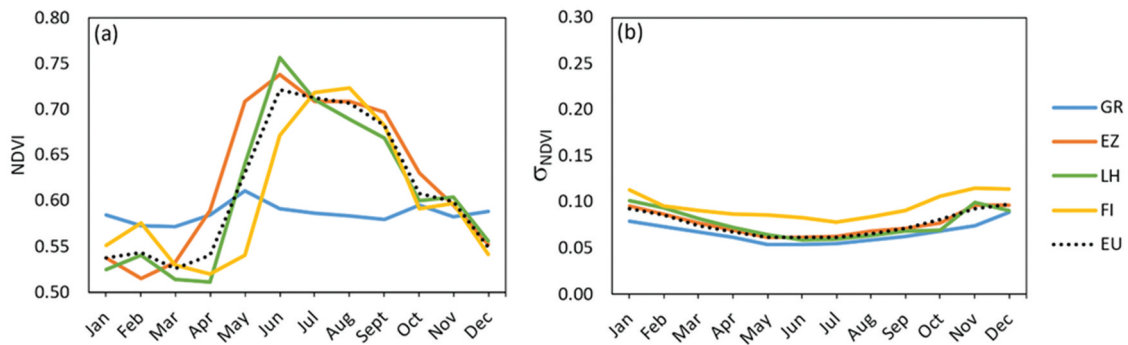


Figure 9. (a) Average NDVI temporal profile in FAs; (b) average σ_{NDVI} temporal profile over FAs.

spatial heterogeneity) than in summer (higher homogeneity). This phenomenon could be related to the vegetative behaviour of vegetation in different areas of Europe. In fact, during winter, local climatic conditions enhance differences that in summer, conversely, appear to be more homogeneous since vegetation reaches its maximum phenological development everywhere (Chmielewski & Rötzer, 2000; Sarvia et al., 2021a). Concerning Figure 8c, it can be highlighted that NDRE uncertainty shows the highest variability; differently, NBR uncertainty shows the lowest one (Figure 8b).

Since at European level averaged values of both VI and σ_{VI} could not be representative of all European local conditions, with reference to FAs, authors computed the correspondent trends and compared them with the European average one (Figure 9).

In particular in Figure 9a, it can be noted that the Europe average NDVI profile well fits the one of Czech Republic, Lithuania and Finland. Conversely, it appears to be not compliant with the one from Greece that shows a slightly stable NDVI profile oscillating around 0.6. This could be probably related to the Mediterranean scrubland vegetation type that characterizes Greece (Rodwell et al., 2002; Zinke, 1973). Other minor differences can additionally be observed: (i) Finland NDVI profile suggests a shorter growing season length mainly due to the start of season delay respect to EU one. In fact, the growing season seems to start around May–June while EU on April–May; (ii) Czech Republic NDVI profile suggests a longer growing season length probably due to earlier start of season and delay of the end of season if compared to EU NDVI profile; (iii) Lithuania’s NDVI profile appears very similar to the European one. These findings are consistent with existing literature. In fact, climate and latitude are known to significantly affect vegetation phenology (Didan & Huete, 2004; Wu et al., 2015; Yu et al., 2003). As highlighted in Figure 9b, NDVI uncertainty appears to be higher during the winter period ($\sigma_{NDVI} \approx 0.10$) while decrease in summer ($\sigma_{NDVI} \approx 0.06$) confirming once again the phenomenon reported in Figures 5 and 6. Moreover, it can

be noted that NDVI uncertainty at European level is similar to other FAs in most cases, although Finland’s uncertainty appears to be higher. This result suggests that the computed EU average σ_{NDVI} is representative of FA and poorly affected by latitudinal gradient. It is worth to stress that NDVI profiles were not used to compare phenology of different countries. In fact, it is well known that latitude strongly influences climate and therefore vegetation characteristics (as proved in Figure 9a). Surprisingly, no significant differences were found in the σ_{NDVI} profiles. Finally, our results show that latitudinal gradient affects NDVI profile but not significantly its uncertainty profile.

In this work, different vegetation types (herbaceous/crops/forests) were merged to better explore VI uncertainty spatiotemporal variability. In fact, merging all vegetated classes allows to mitigate vegetation type-related effects and highlight a general trend over vegetated areas. Nevertheless, further developments will be expected to test the dependence of VI uncertainty to vegetation types.

Conclusions

In this work, the theoretical uncertainty of most common used VIs was explored by some simulation adopting VPL. In particular, NDVI, NBR and NDRE were chosen as the representative of a wider group of S2-derived indices for change detection and phenology monitoring purposes over vegetation (including forests and crops). Subsequently, the VI uncertainty was mapped and assessed pixel-by-pixels using GEE over the EU. The uncertainty variability along time was then assessed, with special concern on the entire 2020. Results proved that a latitudinal gradient was not so evident over FA, suggesting that the estimated EU average uncertainties well represent a general continental behaviour. To give a practical application of derived deductions, VPL was adopted in a change detection framework involving S2-derived VIs. In the latter, one can wonder about the sensibility to appreciate significant difference when comparing two acquisitions. An example was given considering two NDVI

maps (June 2020–September 2020). The σ_{NDVI} for each acquisition was further propagated along difference computation providing a map of final $\Delta NDVI$ uncertainty. The results proved that considering only the SD, about 64% of $\Delta NDVI$ vegetated pixels were masked out. This approach is expected to alert the final user about the reliability of the deductions while working with VI differences in change detection context.

Disclosure statement

No potential conflict of interest was reported by the author(s).

ORCID

S. De Petris  <http://orcid.org/0000-0001-8184-9871>
 F Sarvia  <http://orcid.org/0000-0003-4556-446X>
 E. Borgogno-Mondino  <http://orcid.org/0000-0003-4570-8013>

References

- Anaya, J. A., Chuvieco, E., & Palacios-Orueta, A. (2009). Aboveground biomass assessment in Colombia: A remote sensing approach. *Forest Ecology and Management*, 257(4), 1237–1246. <https://doi.org/10.1016/j.foreco.2008.11.016>
- Beck, P. S. A., Jönsson, P., Høgda, K.-A., Karlsen, S. R., Eklundh, L., & Skidmore, A. K. (2007). A ground-validated NDVI dataset for monitoring vegetation dynamics and mapping phenology in Fennoscandia and the Kola Peninsula. *International Journal of Remote Sensing*, 28(19), 4311–4330. <https://doi.org/10.1080/01431160701241936>
- Borgogno-Mondino, E., Lessio, A., & Gomasasca, M. A. (2016). A fast operative method for NDVI uncertainty estimation and its role in vegetation analysis. *European Journal of Remote Sensing*, 49(1), 137–156. <https://doi.org/10.5721/EuJRS20164908>
- Buchhorn, M., Bertels, L., Smets, B., De Roo, B., Lesiv, M., Tsendbazar, N.-E., Masiliunas, D., & Li, L. (2020). Copernicus Global Land Service: Land Cover 100m: Version 3 Globe 2015-2019: Algorithm theoretical basis document. <https://zenodo.org/record/4723924>
- Burgan, R. E. (1993). *Monitoring vegetation greenness with satellite data* (Vol. 297). US Department of Agriculture, Forest Service, Intermountain Research Station.
- Büttner, G. (2014). CORINE land cover and land cover change products. In *Land use and land cover mapping in Europe* (pp. 55–74). Springer Netherlands. https://doi.org/10.1007/978-94-007-7969-3_5
- Chen, J. M. (1996). Evaluation of vegetation indices and a modified simple ratio for boreal applications. *Canadian Journal of Remote Sensing*, 22(3), 229–242. <https://doi.org/10.1080/07038992.1996.10855178>
- Chen, X., Vogelmann, J. E., Rollins, M., Ohlen, D., Key, C. H., Yang, L., Huang, C., & Shi, H. (2011). Detecting post-fire burn severity and vegetation recovery using multitemporal remote sensing spectral indices and field-collected composite burn index data in a ponderosa pine forest. *International Journal of Remote Sensing*, 32(23), 7905–7927. <https://doi.org/10.1080/01431161.2010.524678>
- Chmielewski, F.-M., & Rötzer, T. (2000). Phenological trends in Europe in relation to climatic changes. *Inst für Pflanzenbauwissenschaften*. https://www.agrar.hu-berlin.de/en/institut-en/departments/dntw-en/agrarmet-en/service/sr_sr_docs/schrift07.pdf
- Curran, P. J. (1981). *Multispectral remote sensing for estimating biomass and productivity*. Plants and the Daylight Spectrum.
- De Petris, S., Sarvia, F., & Borgogno-Mondino, E. (2020). A new index for assessing tree vigour decline based on Sentinel-2 multitemporal data. *Appl Tree Failure Risk Manag. Remote Sens Letters*.
- De Petris, S., Sarvia, F., & Borgogno-Mondino, E. (2021). Multi-temporal mapping of flood damage to crops using Sentinel-1 imagery: A case study of the Sesia River (October 2020). *Remote Sensing Letters*, 12(5), 459–469. <https://doi.org/10.1080/2150704X.2021.1890262>
- De Petris, S., Sarvia, F., Gullino, M., Tarantino, E., & Borgogno-Mondino, E. (2021). Sentinel-1 polarimetry to map apple orchard damage after a storm. *Remote Sensing*, 13(5 (January)), 1030. <https://doi.org/10.3390/rs13051030>
- Didan, K., & Huete, A. 2004. Analysis of the global vegetation dynamic metrics using MODIS vegetation index and land cover products. In IGARSS 2004. 2004 IEEE International Geoscience and Remote Sensing Symposium, Anchorage, Alaska, USA, 3:2058–2061. IEEE.
- Doxani, G., Vermote, E., Roger, J.-C., Gascon, F., Adriaensen, S., Frantz, D., Hagolle, O., Hollstein, A., Kirches, G., & Li, F. (2018). Atmospheric correction inter-comparison exercise. *Remote Sensing*, 10(2), 352. <https://doi.org/10.3390/rs10020352>
- Drusch, M., Del Bello, U., Carlier, S., Colin, O., Fernandez, V., Gascon, F., Hoersch, B., Isola, C., Laberinti, P., Martimort, P., Meygret, A., Spoto, F., Sy, O., Marchese, F., & Bargellini, P. (2012). Sentinel-2: ESA's optical high-resolution mission for GMES operational services. *Remote Sensing of Environment*, 120, 25–36. <https://doi.org/10.1016/j.rse.2011.11.026>
- Escuin, S., Navarro, R., & Fernandez, P. (2008). Fire severity assessment by using NBR (normalized burn ratio) and NDVI (normalized difference vegetation index) derived from LANDSAT TM/ETM images. *International Journal of Remote Sensing*, 29(4), 1053–1073. <https://doi.org/10.1080/01431160701281072>
- Filipponi, F. 2018. BAI2: Burned Area Index for Sentinel-2. In Multidisciplinary Digital Publishing Institute Proceedings, 2:364.
- Fitzgerald, G. J., Rodriguez, D., Christensen, L. K., Belford, R., Sadras, V. O., & Clarke, T. R. (2006). Spectral and thermal sensing for nitrogen and water status in rainfed and irrigated wheat environments. *Precision Agriculture*, 7(4), 233–248. <https://doi.org/10.1007/s11119-006-9011-z>
- Gao, B.-C. (1996). NDWI—A normalized difference water index for remote sensing of vegetation liquid water from space. *Remote Sensing of Environment*, 58(3), 257–266. [https://doi.org/10.1016/S0034-4257\(96\)00067-3](https://doi.org/10.1016/S0034-4257(96)00067-3)
- García, M. L., & Caselles, V. (1991). Mapping burns and natural reforestation using thematic mapper data. *Geocarto International*, 6(1), 31–37. <https://doi.org/10.1080/10106049109354290>
- Gorelick, N., Hancher, M., Dixon, M., Ilyushchenko, S., Thau, D., & Moore, R. (2017). Google Earth Engine:

- Planetary-scale geospatial analysis for everyone. *Remote Sensing of Environment*, 202, 18–27. <https://doi.org/10.1016/j.rse.2017.06.031>
- Govender, M., Chetty, K., & Bulcock, H. (2007). A review of hyperspectral remote sensing and its application in vegetation and water resource studies. *Water Sa*, 33(2), 145–151. <https://doi.org/10.4314/wsa.v33i2.49049>
- Goward, S. N. (1989). Satellite bioclimatology. *Journal of Climate*, 2(7), 710–720. [https://doi.org/10.1175/1520-0442\(1989\)002<0710:SB>2.0.CO;2](https://doi.org/10.1175/1520-0442(1989)002<0710:SB>2.0.CO;2)
- Grabska, E., Hostert, P., Pflugmacher, D., & Ostapowicz, K. (2019). Forest stand species mapping using the Sentinel-2 time series. *Remote Sensing*, 11(10), 1197. <https://doi.org/10.3390/rs11101197>
- Guliyeva, S. H. (2020). Land cover/land use monitoring for agriculture features classification. The International Archives of Photogrammetry. *Remote Sensing & Spatial Information Sciences*, 43, 61–65. <https://doi.org/10.5194/isprs-archives-XLIII-B3-2020-61-2020>
- Holben, B. N., Eck, T. F., Al Slutsker, I., Tanre, D., Buis, J. P., Setzer, A., Vermote, E., Reagan, J. A., Kaufman, Y. J., Nakajima, T., Lavenu, F., Jankowiak, I., & Smirnov, A. (1998). AERONET—A federated instrument network and data archive for aerosol characterization. *Remote Sensing of Environment*, 66(1), 1–16. [https://doi.org/10.1016/S0034-4257\(98\)00031-5](https://doi.org/10.1016/S0034-4257(98)00031-5)
- Huemmerich, K. F., & Goward, S. N. (1992). Spectral vegetation indexes and the remote sensing of biophysical parameters. In IGARSS '92 International Geoscience and Remote Sensing Symposium, 26–29 May 1992, Houston, TX, USA: IEEE. <https://doi.org/10.1109/IGARSS.1992.578329>
- Immitzer, M., Vuolo, F., & Atzberger, C. (2016). First experience with Sentinel-2 data for crop and tree species classifications in Central Europe. *Remote Sensing*, 8(3), 166. <https://doi.org/10.3390/rs8030166>
- Kanjir, U., Djurić, N., & Veljanovski, T. (2018). Sentinel-2 based temporal detection of agricultural land use anomalies in support of common agricultural policy monitoring. *ISPRS International Journal of Geo-Information*, 7(10), 405. <https://doi.org/10.3390/ijgi7100405>
- Karnieli, A., Agam, N., Pinker, R. T., Anderson, M., Imhoff, M. L., Gutman, G. G., Panov, N., & Goldberg, A. (2010). Use of NDVI and land surface temperature for drought assessment: Merits and limitations. *Journal of Climate*, 23(3), 618–633. <https://doi.org/10.1175/2009JCLI2900.1>
- Liaghat, S., & Balasundram, S. K. (2010). A review: The role of remote sensing in precision agriculture. *American Journal of Agricultural and Biological Sciences*, 5(1), 50–55. <https://doi.org/10.3844/ajabssp.2010.50.55>
- Li, F., Miao, Y., Feng, G., Yuan, F., Yue, S., Gao, X., Liu, Y., Liu, B., Ustin, S. L., & Chen, X. (2014). Improving estimation of summer maize nitrogen status with red edge-based spectral vegetation indices. *Field Crops Research*, 157, 111–123. <https://doi.org/10.1016/j.fcr.2013.12.018>
- Louis, J., Debaecker, V., Pflug, B., Main-Knorn, M., Bieniarz, J., Mueller-Wilm, U., Cadau, E., & Gascon, F. (2016). SENTINEL-2 SEN2COR: L2A Processor for users. In: Proceedings Living Planet Symposium 2016, SP-740, pp. 1–8. Proceedings Living Planet Symposium 2016, SP-740, 1–8 May, Prague, Czech Republic.
- Louis, J., Pflug, B., Main-Knorn, M., Debaecker, V., Mueller-Wilm, U., Iannone, R. Q., Cadau, E. G., Boccia, V., & Gascon, F. 2019. Sentinel-2 global surface reflectance level-2A product generated with Sen2Cor. In IGARSS 2019-2019 IEEE International Geoscience and Remote Sensing Symposium, 8522–8525, Yokohama, Japan. IEEE.
- Maes, W. H., & Steppe, K. (2019). Perspectives for remote sensing with unmanned aerial vehicles in precision agriculture. *Trends in Plant Science*, 24(2), 152–164. <https://doi.org/10.1016/j.tplants.2018.11.007>
- Main-Knorn, M., Pflug, B., Louis, J., Debaecker, V., Müller-Wilm, U., & Gascon, F. (2017). Sen2Cor for Sentinel-2. In Lorenzo, B. (Eds.), *Image and Signal Processing for remote sensing XXIII* (Vol. 10427, p. 1042704). International Society for Optics and Photonics.
- Malenovsky, Z., Rott, H., Cihlar, J., Schaepman, M. E., García-Santos, G., Fernandes, R., & Berger, M. (2012). Sentinels for science: Potential of Sentinel-1, -2, and -3 missions for scientific observations of ocean, cryosphere, and land. *Remote Sensing of Environment*, 120, 91–101. <https://doi.org/10.1016/j.rse.2011.09.026>
- Malingreau, J. P. (1989). The vegetation index and the study of vegetation dynamics. In *Applications of remote sensing to agrometeorology* (pp. 285–303). Springer Netherlands. https://doi.org/10.1007/978-94-009-2235-8_12
- Martinelli, F., Scalenghe, R., Davino, S., Panno, S., Scuderi, G., Ruisi, P., Villa, P., Stroppiana, D., Boschetti, M., & Goulart, L. R. (2015). Advanced methods of plant disease detection. *A Review Agronomy for Sustainable Development*, 35(1), 1–25. <https://doi.org/10.1007/s13593-014-0246-1>
- McKean, J., Buechel, S., & Gaydos, L. (1991). Remote sensing and landslide hazard assessment. *Photogrammetric Engineering and Remote Sensing*, 57(9), 1185–1193.
- Misra, G., Cawkwell, F., & Wingler, A. (2020). Status of phenological research using Sentinel-2 data: A review. *Remote Sensing*, 12(17), 2760. <https://doi.org/10.3390/rs12172760>
- Mutanga, O., & Kumar, L. (2019). *Google Earth Engine applications. Remote sensing*. Multidisciplinary Digital Publishing Institute.
- Navarro, A., Catalao, J., & Calvao, J. (2019). Assessing the use of Sentinel-2 time series data for monitoring cork oak decline in Portugal. *Remote Sensing*, 11(21), 2515. <https://doi.org/10.3390/rs11212515>
- Nilsson, H. (1995). Remote sensing and image analysis in plant pathology. *Annual Review of Phytopathology*, 33(1), 489–528. <https://doi.org/10.1146/annurev.py.33.090195.002421>
- Ormsby, J. P., Choudhury, B. J., & Owe, M. (1987). Vegetation spatial variability and its effect on vegetation indices. *International Journal of Remote Sensing*, 8(9), 1301–1306. <https://doi.org/10.1080/01431168708954775>
- Peters, A. J., Griffin, S. C., Viña, A., & Ji, L. (2000). Use of remotely sensed data for assessing crop hail damage. *PE&RS, Photogrammetric Engineering & Remote Sensing*, 66(11), 1349–1355.
- Phiri, D., Simwanda, M., Salekin, S., Nyirenda, V. R., Murayama, Y., & Ranagalage, M. (2020). Sentinel-2 data for land cover/use mapping: A review. *Remote Sensing*, 12 (14 (January)), 2291. <https://doi.org/10.3390/rs12142291>
- Potter, C. S., & Brooks, V. (1998). Global analysis of empirical relations between annual climate and seasonality of NDVI. *International Journal of Remote Sensing*, 19(15), 2921–2948. <https://doi.org/10.1080/014311698214352>
- Price, J. C. (1992). Estimating vegetation amount from visible and near infrared reflectances. *Remote Sensing of Environment*, 41(1), 29–34. [https://doi.org/10.1016/0034-4257\(92\)90058-R](https://doi.org/10.1016/0034-4257(92)90058-R)

- Quintano, C., Fernández-Manso, A., & Fernández-Manso, O. (2018). Combination of Landsat and Sentinel-2 MSI data for initial assessing of burn severity. *International Journal of Applied Earth Observation and Geoinformation*, 64, 221–225. <https://doi.org/10.1016/j.jag.2017.09.014>
- Rodwell, J. S., Schaminée, J. H. J., Mucina, L., Pignatti, S., Dring, J., & Moss, D. (2002). The diversity of European vegetation. An overview of phytosociological alliances and their relationships to EUNIS habitats. Report EC-LNV 54.
- Rouse, J. W., Haas, R. H., Schell, J. A., Deering, D. W., & Harlan, J. C. (1974). Monitoring the vernal advancement and retrogradation (green wave effect) of natural vegetation. NASA/GSFC Type III Final Report, Greenbelt, Md 371.
- Sanyal, J., & Lu, X. X. (2004). Application of remote sensing in flood management with special reference to monsoon Asia: A review. *Natural Hazards*, 33(2), 283–301. <https://doi.org/10.1023/B:NHAZ.0000037035.65105.95>
- Sarvia, F., De, P. S., & Borgogno, M. E. (2020). Multi-scale remote sensing to support insurance policies in agriculture: From mid-term to instantaneous deductions. *GIScience & Remote Sensing*, 57(6), 770–784. <https://doi.org/10.1080/15481603.2020.1798600>
- Sarvia, F., De Petris, S., & Borgogno-Mondino, E. (2019). Remotely sensed data to support insurance strategies in agriculture. In Christopher, M. U. Neale, Antonino, M. *Remote sensing for agriculture, ecosystems, and hydrology XXI* (Vol. 11149, p. 111491H). International Society for Optics and Photonics.
- Sarvia, F., De Petris, S., & Borgogno-Mondino, E. (2020). A methodological proposal to support estimation of damages from hailstorms based on Copernicus Sentinel 2 data times series. In International Conference on Computational Science and Its Applications, 737–751. Springer.
- Sarvia, F., De Petris, S., & Borgogno-Mondino, E. (2021a). Exploring climate change effects on vegetation phenology by MOD13Q1 data: The Piemonte region case study in the Period 2001–2019. [*L R Br*] *Agronomy*, 11(3), 555. <https://doi.org/10.3390/agronomy11030555>
- Sarvia, F., De Petris, S., & Borgogno-Mondino, E. (2021b, March). Exploring climate change effects on vegetation phenology by MOD13Q1 data: The Piemonte region case study in the Period 2001–2019. [*L R Br*] *Agronomy*, 11(3), 555. <https://doi.org/10.3390/agronomy11030555>
- Sarvia, F., Xausa, E., Petris, S. D., Cantamessa, G., & Borgogno-Mondino, E. (2021). A possible role of Copernicus Sentinel-2 data to support common agricultural policy controls in agriculture. [*L R Br*] *Agronomy*, 11(1), 110. <https://doi.org/10.3390/agronomy11010110>
- Segarra, J., Buchaillet, M. L., Araus, J. L., & Kefauver, S. C. (2020). Remote sensing for precision agriculture: Sentinel-2 improved features and applications. [*L R Br*] *Agronomy*, 10(5), 641. <https://doi.org/10.3390/agronomy10050641>
- Sentinel, E. S. A. (2014). *3-missions-sentinel online*. ESA.
- Sinha, S., Jeganathan, C., Sharma, L. K., & Nathawat, M. S. (2015). A review of radar remote sensing for biomass estimation. *International Journal of Environmental Science and Technology*, 12(5), 1779–1792. <https://doi.org/10.1007/s13762-015-0750-0>
- Smirnov, A., Holben, B. N., Eck, T. F., Dubovik, O., & Slutsker, I. (2000). Cloud-screening and quality control algorithms for the AERONET Database. *Remote Sensing of Environment*, 73(3), 337–349. [https://doi.org/10.1016/S0034-4257\(00\)00109-7](https://doi.org/10.1016/S0034-4257(00)00109-7)
- Sripada, R. P., Heiniger, R. W., White, J. G., & Weisz, R. (2005). Aerial color infrared photography for determining late-season nitrogen requirements in corn. *Agronomy Journal*, 97(5), 1443–1451. <https://doi.org/10.2134/agronj2004.0314>
- Vermote, E., Doxani, G., Gascon, F., & Roger, J.-C. (2019). ACIX—atmospheric correction inter-comparison EXercise. In IGARSS 2019-2019 IEEE International Geoscience and Remote Sensing Symposium, 8493–8496, Yokohama, Japan. IEEE.
- Vermote, E. F., Tanré, D., Deuze, J. L., Herman, M., & Morcette, J.-J. (1997). Second simulation of the satellite signal in the solar spectrum, 6S: An overview. *IEEE Transactions on Geoscience and Remote Sensing*, 35(3), 675–686. <https://doi.org/10.1109/36.581987>
- Wang, Q., Adiku, S., Tenhunen, J., & Granier, A. (2005). On the relationship of NDVI with leaf area index in a deciduous forest site. *Remote Sensing of Environment*, 94(2), 244–255. <https://doi.org/10.1016/j.rse.2004.10.006>
- Wardlow, B. D., Anderson, M. C., and Verdin, J. P., Wardlow, B. D., Anderson, M. C., Verdin, J. P. (2012). *Remote sensing of drought: Innovative monitoring approaches*. CRC Press. <https://doi.org/10.1201/b11863>
- Weiss, M., Jacob, F., & Duveiller, G. (2020). Remote sensing for agricultural applications: A meta-review. *Remote Sensing of Environment*, 236, 111402. <https://doi.org/10.1016/j.rse.2019.111402>
- West, H., Quinn, N., & Horswell, M. (2019). Remote sensing for drought monitoring & impact assessment: Progress, past challenges and future opportunities. *Remote Sensing of Environment*, 232, 111291. <https://doi.org/10.1016/j.rse.2019.111291>
- Wu, D., Zhao, X., Liang, S., Zhou, T., Huang, K., Tang, B., & Zhao, W. (2015). Time-lag effects of global vegetation responses to climate change. *Global Change Biology*, 21(9), 3520–3531. <https://doi.org/10.1111/gcb.12945>
- Xiao, J., & Moody, A. (2005). A comparison of methods for estimating fractional green vegetation cover within a desert-to-upland transition zone in Central New Mexico, USA. *Remote Sensing of Environment*, 98(2–3), 237–250. <https://doi.org/10.1016/j.rse.2005.07.011>
- Xie, Y., Sha, Z., & Yu, M. (2008). Remote sensing imagery in vegetation mapping: A review. *Journal of Plant Ecology*, 1(1), 9–23. <https://doi.org/10.1093/jpe/rtm005>
- Xue, J., & Su, B. (2017). Significant remote sensing vegetation indices: A review of developments and applications. *Journal of Sensors*, 2017, 1–17. <https://doi.org/10.1155/2017/1353691>
- Yu, F., Price, K. P., Ellis, J., & Shi, P. (2003). Response of seasonal vegetation development to climatic variations in Eastern Central Asia. *Remote Sensing of Environment*, 87(1), 42–54. [https://doi.org/10.1016/S0034-4257\(03\)00144-5](https://doi.org/10.1016/S0034-4257(03)00144-5)
- Zhang, X., Friedl, M. A., Schaaf, C. B., Strahler, A. H., Hodges, J. C., Gao, F., Reed, B. C., & Huete, A. (2003). Monitoring vegetation phenology using MODIS. *Remote Sensing of Environment*, 84(3), 471–475. [https://doi.org/10.1016/S0034-4257\(02\)00135-9](https://doi.org/10.1016/S0034-4257(02)00135-9)
- Zhang, B., Wu, D., Zhang, L., Jiao, Q., & Li, Q. (2012). Application of hyperspectral remote sensing for environmental monitoring in mining areas. *Environmental Earth Sciences*, 65(3), 649–658. <https://doi.org/10.1007/s12665-011-1112-y>
- Zinke, P. J. (1973). Analogies between the soil and vegetation types of Italy, Greece, and California. In *Mediterranean type ecosystems* (pp. 61–80). Springer Berlin Heidelberg. https://doi.org/10.1007/978-3-642-65520-3_6